# Elastic-Plastic Finite Element Analysis of Automotive Body Panel Stamping Processes Using Dynamic Explicit Time Integration Scheme

*D.W. Jung and D.Y. Yang*

*(Submitted 2 June 1998; in revised form 25 June 1999)*

**In this article, the elastic-plastic finite element formulations using dynamic explicit time-integration schemes are proposed for numerical analysis of automotive body panel stamping processes. A general formulation of finite element simulation for complex sheet forming processes with arbitrarily shaped tools is briefly introduced. In finite element simulation of automotive body panel stamping processes, the robustness and stability of computation are important requirements since the computation time and convergency become major points of consideration besides the solution accuracy due to the complexity of geometry and boundary conditions. For analyses of more complex cases with larger and more refined meshes, the explicit method is more time effective than the implicit method, and it has no convergency problem and has the robust nature of contact and friction algorithms, although the implicit method is widely used because of excellent accuracy and reliability. The elastic-plastic scheme is more reliable and rigorous, while the rigid-plastic scheme requires short computation time. The performance of the dynamic explicit algorithms is investigated by comparing the simulation results of forming of complex-shaped automotive body parts, such as a fuel tank and a rear hinge, with the experimental results. It has been shown that dynamic explicit schemes provide quite similar results to the experimental results. It is thus shown that the proposed dynamic explicit elastic-plastic finite element method enables an effective computation for complicated automotive body panel stamping processes.**

**Keywords** automotive body panel stamping, dynamic explicit, elastic-plastic, finite element method, sheet metal forming

## 1. Introduction

It is possible nowadays to simulate numerically, with good accuracy, sheet forming processes with simple geometries and small changes in contact surfaces; therefore, such examples appear in abundance in the literature. Despite this success, there is still a great deal of effort necessary to develop a reliable and cost-effective algorithm for practical analysis of industrial problems to treat complex, irregularly curved geometries and large relative displacements between sheet material and dies. The methods used successfully for simple simulations may not always be useful for more complex problems. Finally, efficiency and robustness of the solution are very important, and this problem cannot be solved simply, even if the more advanced computers are used.

During the last decade, a tremendous increase in the number of papers treating finite element simulation of sheet metal forming has been seen. In the later part of the period, a move away from static implicit finite element methods (FEMs) to dynamic explicit FEMs has appeared. The main reason why the explicit technique has so rapidly come into focus, both in the academic world and in industry, is quite obvious. A general sheet metal forming process can be characterized as being, to a high degree, a nonlinear event. This is not only due to geometric and material nonlinearity, but also to variation in the contact conditions. Traditional instabilities occurring in the typical deep-drawing process—formation of wrinkles and necking—also give rise to additional nonlinear effects. Due to these strong nonlinear effects, the implicit methods often fail to converge, whereas the explicit integration technique does not contain this pitfall; it always leads to a solution.

The explicit dynamic algorithm has several significant advantages over a conventional implicit static algorithm for the sheet metal forming processes. First, in the explicit method, there is no banded equation solver like Newton-Raphson method. Consequently, the computational cost of a solution does not grow quadratically with the problem size. In general, the computational cost increases linearly depending on the problem size of the explicit dynamic procedure. Second, large deformation, sliding, and three-dimensional contact constraints are relatively easy to implement in the explicit procedure.

The kinematic contact constraints can be enforced explicitly like the direct trial-and-error method, since there is no equation solver available and changing contact conditions do not require bandwidth optimization considerations. The major disadvantage of the explicit dynamic procedure is the possible static instability of a solution to the time- and rate-dependent dynamic procedure. Generally, this requires the artificial time scaling for the analysis to achieve an economical solution. Typically, the dynamic sheet metal forming analysis is performed at punch velocities around the order of 5 to 20 m/s, under the assumption of the near-quasi-static solutions.

**D.W. Jung,** Department of Mechanical Engineering, Cheju National University, Cheju-Do, 690-756 Korea; and **D.Y. Yang,** Department of Mechanical Engineering, KAIST, Taejon, Korea. Contact e-mail: jdwcheju@cheju.cheju.ac.kr.

During the last decade, two major approaches have usually been employed in analyzing the large deformation of sheet metals FEM, rigid-plastic FEM and elastic-plastic FEM, depending on the type of constitutive laws. In the rigid-plastic FEM, the elastic strain is ignored. It is not necessary to check the yield condition during the computation procedure, and thus the computing time can be greatly reduced. These advantages have made the rigid-plastic FEM better for analyzing the metal forming process in spite of some numerical drawbacks. Despite the practical efficiency of the rigid-plastic FEM, it suffers a severe drawback in that it fails to predict the stress history whenever elastic loading or unloading from the plastic state is encountered. Accurate computations of the complete stress and the deformation history are useful in predicting the final mechanical properties of the product and the possible defects in it. In addition, the rigid-plastic FEM is inappropriate for problems involving a significant effect of elastic unloading. In sheet metal forming, the amount of elastically recovered displacement is relatively large even though the elastically recovered strain is small, because the dimension of thickness is much smaller than other dimensions of the sheet metal.

The material model influencing efficiency and possibly also numerical stability is an important part of the algorithm. In metal forming applications, both rigid-plastic and elastic-plastic models have been utilized. The application of elastic-plastic relations for metal forming was dated from earlier papers by Lee and Kobayashi (Ref 1) and Wang and Budiansky (Ref 2) and was connected with the "solid" approach. It is well-known that the elastic-plastic models are less time efficient than the rigid-plastic models because of their greater complexity. The formulations and solution methods used, although based on the general idea of the FEM, constitute by no means a single approach. The major issues to be decided when developing the formulation of the forming code include choice of general solution method (implicit or explicit), "solid" or "flow" formulation, frictional contact models, and material models, among others.

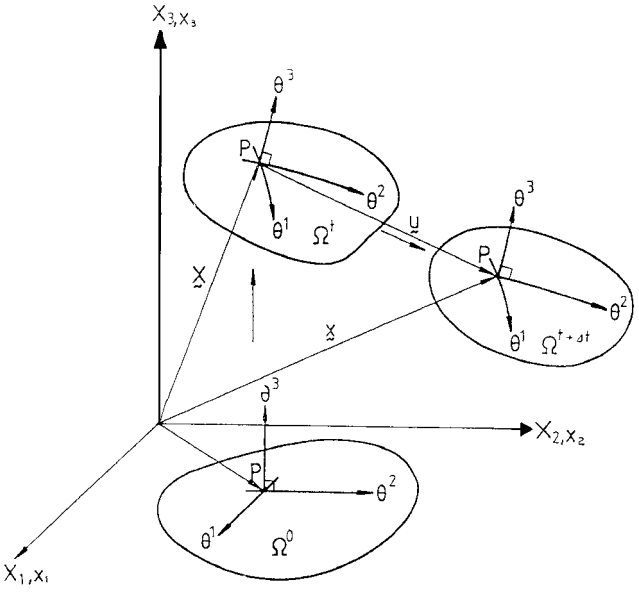


**Fig. 1** Convected coordinate system in the deformation process

This article concentrates on one of several choices, namely for the elastic-plastic material model, and investigates the influence of this model on the performance of the dynamic explicit simulation of sheet forming processes. The performance of the proposed elastic-plastic algorithm is investigated, and the numerical results are compared to the results of experiment. This is followed by a discussion and conclusions concerning accuracy, robustness, and efficiency of the tested models.

The practical application of the finite element method to a full three-dimensional problem is still difficult due to large computation time, complexity in contact treatment, unknown boundary conditions, huge amount of time-consuming tool data preparation, and so forth.

## 2. Elastic-Plastic Constitutive Equations

A deformed body is considered in three-dimensional space (Fig. 1). In analyzing the nonsteady-state deformation by a step-by-step procedure, consider the deformation during one step from time $t_0$ to time $t_0 + \Delta t$.

In Fig. 1, $\theta^1$ and $\theta^2$ are taken as the surface convected coordinates, and the $\theta^3$ axis is taken to be the direction normal to the sheet surface. Let $G_{\alpha\beta}$ and $g_{\alpha\beta}$ be the metric tensors of the undeformed and deformed configurations and let $G^{\alpha\beta}$ and $g^{\alpha\beta}$ be their respective inverses. Base vectors in the undeformed configuration are denoted by $E_\alpha$ and their reciprocals by $E^\alpha$. Similarly, the base vectors in the deformed body are denoted by $e_\alpha$ and their reciprocals by $e^\alpha$.

$$E_\alpha = \frac{\partial X}{\partial \theta^\alpha} \qquad e_\alpha = \frac{\partial x}{\partial \theta^\alpha} \tag{Eq 1}$$

$$G_{\alpha\beta} = E_\alpha \cdot E_\beta \qquad g_{\alpha\beta} = e_\alpha \cdot e_\beta \tag{Eq 2}$$

$$E^{\alpha\beta} = G^{\alpha\beta} E_\beta \qquad e^\alpha = g^{\alpha\beta} e_\beta \tag{Eq 3}$$

The displacement vector $u$ from the undeformed configuration is:

$$u = u^\alpha E_\alpha = u_\alpha E^\alpha = u_1 E^1 \tag{Eq 4}$$

where $u^\alpha = G^{\alpha\beta} u_\beta$. It is implied that the Greek indices refer to the convected coordinates and Latin indices refer to the rectangular Cartesian coordinates. The Lagrangian strain tensor $\varepsilon$ in the convected coordinates system is then given by:

$$\varepsilon = \varepsilon_{\alpha\beta} E^\alpha E^\beta = \varepsilon^{\alpha\beta} E_\alpha E_\beta \tag{Eq 5}$$

$$\varepsilon_{\alpha\beta} = \frac{1}{2}(g_{\alpha\beta} - G_{\alpha\beta}) = \frac{1}{2}(u_{\alpha,\beta} + u_{\beta,\alpha} + u^\gamma{}_{,\alpha}\, u_{\gamma,\beta}) \tag{Eq 6}$$

where the comma denotes covariant differentiation with respect to the undeformed metric. Decomposing the Lagrangian stress tensor into a linear part and a nonlinear part gives:

$$\varepsilon_{\alpha\beta} = e_{\alpha\beta} + \eta_{\alpha\beta} \quad \text{(Eq 7)}$$

where:

$$e_{\alpha\beta} = \frac{1}{2}(u_{\alpha,\beta} + u_{\beta,\alpha}) \qquad \eta_{\alpha\beta} = \frac{1}{2}u^{\gamma}{}_{,\alpha}\, u_{\gamma,\beta}$$

The updated Lagrangian equation considering the large deformation is given as:

$$\int_{V^o} \Delta S^{\alpha\beta}\delta e_{\alpha\beta} dV + \int_{V^o} \tau^{\alpha\beta} u^k{}_{,\alpha}\, \delta u^k{}_{,\beta}\, dV = \int_{S_t^o} t_i^{(t_o + \Delta t)}\, \delta u_i dS - \int_{V^o} \tau^{\alpha\beta}\delta e_{\alpha\beta} dV \quad \text{(Eq 8)}$$

Detailed derivation for Eq 8 can be found in the Appendix to the work by Shim and Yang (Ref 3).

If the constitutive tensor is taken for the second Piola-Kirchhoff stress increment and Lagrangian strain, then:

$$\Delta S^{\alpha\beta} = L^{\alpha\beta\gamma\rho} e_{\gamma\rho} \quad \text{(Eq 9)}$$

The detailed formulation regarding Eq 9 can be found in the Appendix to the work by Shim and Yang (Ref 3). The components of the elastic-plastic constitutive tensor satisfying Hill's anisotropic yield function, normality, and consistency rule are found as (Ref 4, 5):

$$L^{\alpha\beta\gamma\rho} = \frac{E(1+R)}{1+2R}\left\{\frac{1}{2}(g^{\alpha\gamma}g^{\beta\rho} + g^{\alpha\rho}g^{\beta\gamma}) + Rg^{\alpha\beta}g^{\gamma\rho}\right\} - \Gamma\frac{E^2\tau^{\alpha\beta}\tau^{\gamma\rho}}{\bar{\sigma}^2(E+h')} - \frac{1}{2}(g^{\alpha\gamma}\tau^{\beta\rho} + g^{\beta\gamma}\tau^{\alpha\rho} + g^{\alpha\rho}\tau^{\beta\gamma} + g^{\beta\rho}\tau^{\alpha\gamma}) \quad \text{(Eq 10)}$$

where the Greek indices range over 1 to 2.

Combining Eq 8 and 9, a resultant updated Lagrangian equation is obtained for the elastic-plastic solid:

$$\int_{V^o} L^{\alpha\beta\gamma\rho} e_{\alpha\beta}\delta e_{\gamma\rho} dV + \int_{V^o} \tau^{\alpha\beta}\frac{\partial u_i}{\partial \theta^{\alpha}} \cdot \frac{\partial\, \delta u_i}{\partial \theta^{\beta}} dV = \int_{S_t^o} t_i^{(t_o + \Delta t)}\, \delta u_i dS - \int_{V^o} \tau^{\alpha\beta}\delta e_{\alpha\beta} dV \quad \text{(Eq 11)}$$

As the components of the second Piola-Kirchhoff stress tensor are equal to the components of the Kirchhoff stress tensor in the convected coordinate system, the stress integration procedure is very simple compared with other coordinate systems. Once the approximations to the displacement increments have been calculated using Eq 11, the stress components corresponding to time $t_o + \Delta t$ are calculated using Eq 9.

$$(S^{\alpha\beta})^{(t_o + \Delta t)} = (S^{\alpha\beta})^{t_o} + \Delta S^{\alpha\beta} \quad \text{(Eq 12)}$$

$$(\tau^{\alpha\beta})^{(t_o + \Delta t)} = (S^{\alpha\beta})^{(t_o + \Delta t)} \quad \text{(Eq 13)}$$

The working material can be assumed to be incompressible for plastically deforming solids. Then, the Kirchhoff stress tensor $\tau$ is equal to the Cauchy stress tensor $\sigma$.

## 3. General Description of the Dynamic Explicit Formulation

A nonlinear finite element equation of motion is obtained from the principle of virtual work that is the weak form for equilibrium equation. The weak form, which includes internal force, contact/friction force, inertia force, damping force, external force, and boundary condition, is described as follows (Ref 6):

$$\int_{V^o} S\delta E dv + \int_{V^o} \rho_o \ddot{x}\delta u dv - \int_{V^o} \rho_o b\delta u dv - \int_S F_o \delta u ds + \sum_{i=1}^{1} \int_{S_i} \frac{(P_c^i \delta g_n^i + \tau_c \delta g_T^i)}{\text{Contact+ friction}}\, dS = 0 \quad \text{(Eq 14)}$$

where $S$ means the surface that is subjected to the external force, and $S_i$ means the surface in contact. The left-hand side of Eq 14 includes the terms for internal work, inertia work, work done by body force, work exerted by the stress-boundary condition, and work consumption due to contact and friction. In finite element discretization of Eq 14, the internal work term includes either material behavior model or kinematic model according to element types.

If membrane model, material behavior model, element shape function, and dynamics of rigid body are introduced into the principle of virtual work, a nonlinear finite element equation of motion can be obtained. The nonlinear finite element equation can be expressed by the following matrix form at time step $n$:

$$[M]\{\ddot{u}_n\} + [C]\{\dot{u}_n\} + \{P_n\} + \{F_n\} - \{R_{cn}\} = 0 \quad \text{(Eq 15)}$$

From Eq 15, in order to obtain a solution at time step $n + 1$, the central difference method for the time discretization of acceleration and velocity is introduced:

$$\ddot{u}_n = \frac{\dot{u}_{n+1/2} - \dot{u}_{n-1/2}}{\Delta t} = \frac{u_{n+1} - 2u_n + u_{n-1}}{2\Delta t^2}$$

$$\dot{u}_{n+1/2} = \frac{u_{n+1} - u_n}{\Delta t} \quad \text{or} \quad \dot{u}_n = \frac{u_{n+1} - u_{n-1}}{2\Delta t} \quad \text{(Eq 16)}$$

If Eq 16 is substituted into Eq 15 and rearranged, the following equation can be obtained accordingly:

$$\left(\frac{M}{\Delta t^2}+\frac{C}{2\Delta t}\right)u_{n+1}=F_n-P_n-R_{cn}+\frac{M}{\Delta t^2}u_n-\left(\frac{M}{\Delta t^2}-\frac{C}{2\Delta t}\right)u_{n-1} \quad \text{(Eq 17)}$$

The central difference method has selective convergency according to the magnitude of $\Delta t$, and the accuracy and convergency are linearly proportional to the square of $\Delta t$. Nodal displacements can be obtained at time step $n + 1$ by Eq 17, then the deformation area is updated. A new magnitude of time increment to guarantee convergency should be decided according to the updated deformation. The magnitude of global time increment can be determined by the following equation after calculating the time increment of every element:

$$\Delta t_{n+1}=\alpha \min\left[\Delta t_1, \Delta t_2, \ldots, \Delta t_N\right] \quad \text{(Eq 18)}$$

where $N$ is the total element number and $\Delta t_i$ is the time increment of the $i$th element. Also, the safe constant $\alpha$ has often been selected to be less than 0.9.

The critical time increment is determined as follows:

$$\Delta t_c = L_s/C \quad \text{(Eq 19)}$$

where $L_s$ is the characteristic length that is the given element area divided by the largest edge.

The propagation speed $C$ is determined as:

$$C=\sqrt{\frac{E_t}{\rho}} \quad \text{(Eq 20)}$$

### 3.1 Bending Energy Augmented Membrane Element

In spite of numerous advantages of the membrane theory, the conventional membrane formulation is not appropriate for problems that involve the considerable effect of bending and shape change. Especially in deep drawing with tools of complex geometry, numerical buckling may occur in the course of computation at the free surface of deforming sheet metal, which is not observed in the real forming processes. Therefore, in order to maintain the advantages of membrane elements and to overcome such drawbacks a bending energy augmented membrane (BEAM) element (Ref 7) is used.

### 3.2 Rotational Bending Stiffness for BEAM Element

For the sake of simplicity of conceptual explanation, three nodes lying in one plane are considered; they are connected to each other by simple bar elements, as shown in Fig. 2.

Let $L_1, L_2, n_1, n_2$ be the length and the normal vectors of two bar elements, respectively. Then, the incremental rotated angle between a bar 2-5 and a bar 5-8 during one step can be expressed by:

$$\delta\theta=-\frac{1}{L_1}n_1\cdot u_1-\frac{1}{L_2}n_2\cdot u_2 \quad \text{(Eq 21)}$$

where $u_1$ is the relative displacement vector of node 2 with respect to node 5 and $u_2$ is that of node 8 with respect to node 5.

Then, Eq 21 can be described in the following matrix form:

$$\delta\theta=[n][U]^T \quad \text{(Eq 22)}$$

where:

$$[n]=\left[-\frac{n_{1x}}{L_1},-\frac{n_{1y}}{L_1},-\frac{n_{1z}}{L_1},\frac{n_{1x}}{L_1}+\frac{n_{2x}}{L_2},\frac{n_{1y}}{L_1}+\frac{n_{2y}}{L_2},\frac{n_{1z}}{L_1}+\frac{n_{2z}}{L_2},-\frac{n_{2x}}{L_2},-\frac{n_{2y}}{L_2},-\frac{n_{2z}}{L_2}\right]$$

$$[U]=[u_1, v_1, w_1, u_2, v_2, w_2, u_3, v_3, w_3]$$

For the evaluation of the rotational bending energy with respect to this incremental rotated angle, it is assumed that a rotational spring is included in node 5, whose rotational stiffness is $k_r$, as shown in Fig. 2. Therefore, the rotational bending energy due to this node spring is expressed as:

$$E_b=\frac{1}{2}k_r\delta\theta^2 \quad \text{(Eq 23)}$$

On substituting Eq 22 into Eq 23 and differentiating the resulting equation twice with respect to $[U]$ under the assumption that $k_r$ and $[n]$ are independent of the displacements $[U]$ during one step, the rotational bending stiffness is obtained by:

$$[K]^e_{9\times 9}=K_r[n]^T[n] \quad \text{(Eq 24)}$$

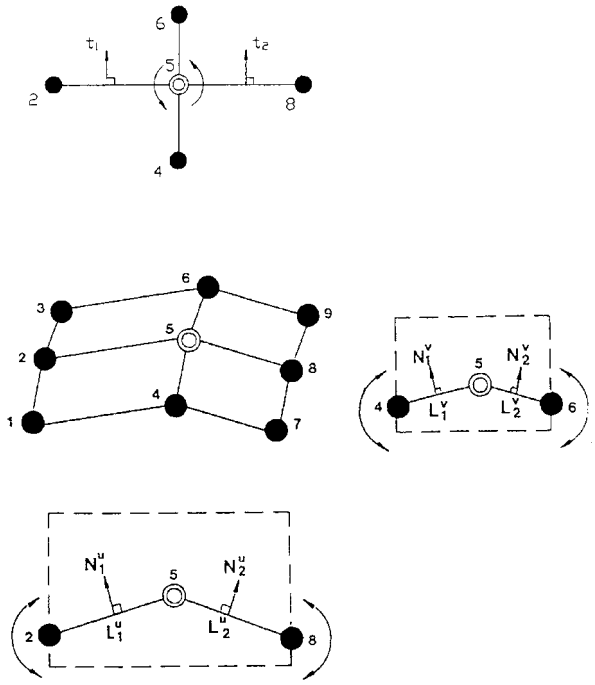


**Fig. 2** Schematic of the in-plane rotational spring and drilling degrees of freedom

From the above considerations, the rotational bending stiffness derived in this way can be described only with respect to the related degrees of freedom of nodes neighboring a node at which there is concern, for example, node 5, without any additional increase in the total number of equations.

### *3.3 Rotational Damping and Spring Applied to the Drilling Direction for Dynamic Analysis*

In dynamic analysis, in order to prevent a zero-energy mode, both in-plane rotational damping and rotational spring are applied in the drilling direction (Ref 6). The same method as applying bending-edge rotational damping is considered, but the tangent vectors are used to obtain a normal vector of the drilling direction. Therefore, in Fig. 2 the drilling angular velocity between bar 2-5 and bar 5-8 during one step can be expressed as:

$$\dot{\delta\theta} = -\frac{1}{L_1} t_1 \cdot \dot{u}_1 - \frac{1}{L_2} t_2 \cdot \dot{u}_2 \qquad \text{(Eq 25)}$$

where $t_1$ and $t_2$ are the tangential vectors of two elements.

Equation 25 can be described in the matrix form as:

$$\dot{\delta\theta} = [t][\dot{U}]^{\mathrm{T}} \qquad \text{(Eq 26)}$$

where

$$[t] = \left[-\frac{t_{1x}}{L_1}, -\frac{t_{1y}}{L_1}, -\frac{t_{1z}}{L_1}, \frac{t_{1x}}{L_1}+\frac{t_{2x}}{L_2}, \frac{t_{1y}}{L_1}+\frac{t_{2y}}{L_2}, \frac{t_{1z}}{L_1}+\frac{t_{2z}}{L_2}, -\frac{t_{2x}}{L_2}, -\frac{t_{2y}}{L_2}, -\frac{t_{2z}}{L_2}\right]$$

$$[\dot{U}] = [\dot{u}_1, \dot{v}_1, \dot{w}_1, \dot{u}_2, \dot{v}_2, \dot{w}_2, \dot{u}_3, \dot{v}_3, \dot{w}_3]$$

Therefore, the damping energy due to the in-plane rotational damping about the drilling direction of a node is expressed as:

$$E_{\mathrm{dd}} = \frac{1}{2} C_{\mathrm{d}} \dot{\delta\theta}^2 \qquad \text{(Eq 27)}$$

The corresponding damping coefficient, $C_{\mathrm{d}}$, is an empirical artificial value that is sufficiently small. The in-plane rotational spring can be considered in a similar manner. The corresponding incremental angle between bar 2-5 and bar 5-8 during one step can be expressed by:

$$\delta\theta = -\frac{1}{L_1} t_1 \cdot u_1 - \frac{1}{L_2} t_2 \cdot u_2 \qquad \text{(Eq 28)}$$

where $u_1$ is the relative displacement vector of node 2 with respect to node 5 and $u_2$ is that of node 8 with respect to node 5.

Then, Eq 28 can be described in the matrix form as:

$$\delta\theta = [t][U]^{\mathrm{T}} \qquad \text{(Eq 29)}$$

Therefore, the bending energy due to this node spring is expressed as:

$$E_{\mathrm{sd}} = \frac{1}{2} K_{\mathrm{d}} \delta\theta^2 \qquad \text{(Eq 30)}$$

The spring coefficient $K_{\mathrm{d}}$ is an empirical artificial value that is sufficiently small. On substituting Eq 29 into Eq 30 and differentiating twice with respect to $[U]$ under the assumption that $K_{\mathrm{d}}$ and $[t]$ are independent of the displacement $[U]$ during one step, the corresponding stiffness is obtained as:

$$[K]^{\mathrm{e}}_{9\times 9} = K_{\mathrm{d}}[t]^{\mathrm{T}}[t] \qquad \text{(Eq 31)}$$

### *3.4 Lumping Scheme*

The computational efficiency and accuracy of the explicit procedure is based on the implementation of an explicit integration rule along with the use of lumped element mass matrices (Ref 8-11).

$$[M][a] = [F], \qquad [a] = [M]^{-1}[F] \qquad \text{(Eq 32)}$$

If matrix $[M]$ is lumped as a diagonal matrix, matrix inversion is not needed, and a solution can be directly obtained by a linear equation, $a_i = m_i^{-1} f_i$. The lumping scheme is computationally economic because matrix inversion involves large computing time. Often in dynamic analysis, the use of lumping mass renders more accurate results than consistent mass.

In this study, the lumping scheme is expressed as:

$$m^{\mathrm{e}}_{pq} = \begin{cases} \alpha\delta_{ij} \int_{\Omega^{\mathrm{e}}} \rho N_a^2 d\Omega, & a = b \\ 0, & a \neq b \end{cases} \qquad \text{(Eq 33)}$$

where

$$\alpha = \frac{\int_{\Omega^{\mathrm{e}}} \rho d\Omega}{\dfrac{\text{(Total element)}}{\sum_{a=1}^{n_{\mathrm{eg}}} \int_{\Omega^{\mathrm{e}}} \rho N_a^2 d\Omega}{\left(\begin{array}{c}\text{Amount of diagonal}\\ \text{entries of consistent mass}\end{array}\right)}}$$

where $\Omega^{\mathrm{e}}$ is element domain, $p$ and $q$ are element equation numbers, and $a$ and $b$ are element node numbers. In this method, lumped mass is proportional to the diagonal part of the consistent mass matrix and the positive valued lumped mass can be always obtained. In the above equation, the constant $\alpha$ is used to conserve the total element mass.

### *3.5 The Efficient Contact and Friction Treatment Scheme for Dynamic Explicit Integration*

The explicit contact algorithm takes advantage of a small time increment required by the stability limit (Ref 8). The use of small increments is advantageous in that it vastly simplifies the implementation of contact conditions.

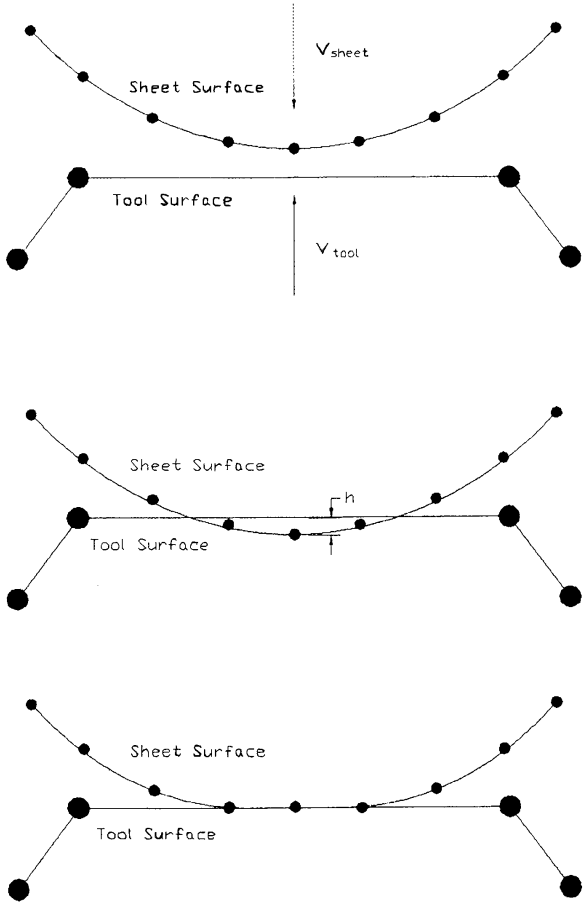


**Fig. 3** Schematic of the contact scheme. (a) Impending contact of two surfaces. (b) Surfaces in predicted configuration. (c) Kinematically compliant surfaces

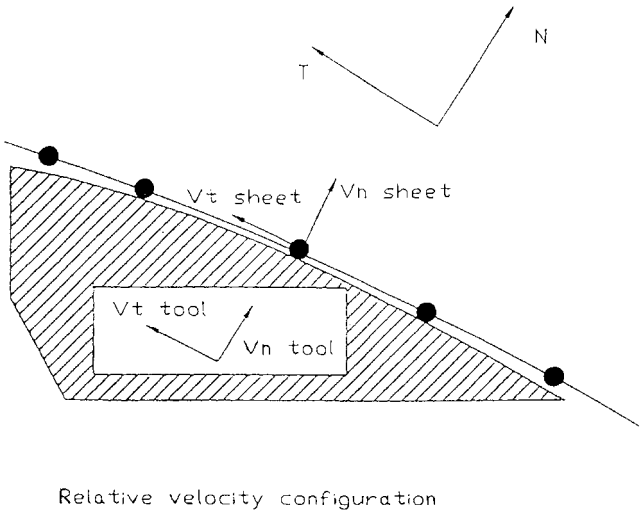


**Fig. 4** Schematic of friction and stick/slip check

In the work described in this article, the contact and friction scheme is the mixed form of the skew boundary condition and the direct trial-and-error method (Ref 9). The accelerations, velocities, and displacements are calculated first without taking the contact conditions into consideration. Then, the penetration distance $h$ and the tool and sheet normal directions of contact points are calculated as in Fig. 3.

From the above calculation, the skew boundary condition is applied and the resisting force to prevent the penetration of a node is readily calculated as:

$$N = mhn/\Delta t^2 \quad \text{(Eq 34)}$$

where $m$ is a nodal lumping mass and $n$ is a normal vector. If it is assumed that the motion of the tools is not influenced by the contact itself, the acceleration changes as:

$$a = a_{\text{pred}} + a_{\text{corr}} = a_{\text{pred}} + N/m \quad \text{(Eq 35)}$$

and the corrections to the velocity and displacement are calculated as:

$$V = V_{\text{pred}} + a_{\text{corr}}\Delta t \qquad u = u_{\text{pred}} + V_{\text{corr}}\Delta t \quad \text{(Eq 36)}$$

For friction, the increment is first solved without taking friction into consideration, and the skew boundary condition is applied in Fig. 4. Under the skew boundary condition, it is not necessary to define a surface direction $t_c$ along which a slip increment $r_c$ is measured. The resisting force $T_c$ required to prevent slip is then calculated in the same way as the calculation of the force required to prevent penetration:

$$T_c = -mr_c/\Delta t^2 \quad \text{(Eq 37)}$$

where $r_c$ is the slip increment.

Accordingly, the friction force is calculated as:

$$T_{\text{frict}} = \frac{T_c}{|T_c|} \min\,(T_{cr}, |T_c|) \quad \text{(Eq 38)}$$

The resisting force $|T_c|$ is compared with the critical force $T_{cr} = \mu|N|$. If the resisting force is less than the critical force, a sticking condition is assumed and then the resisting force is simply applied. If the resisting force is larger than the critical force, a slipping condition is assumed and the friction force is assumed to obey Coulomb's friction law. The procedures of friction force calculation and stick/slip check are summarized in Fig. 5.

## 4. Results and Discussion

### *4.1 Deep Drawing of a Fuel Tank*

A fuel tank is difficult to simulate because the tool surface geometry has embossing in order to impose the rigidity in the middle part of the product, and there exists higher-order nonlinearities of contact and friction. For implicit analysis, the converged results cannot be obtained due to complex geometry including the embossing. The rigid tool is modeled by CATIA computer-aided design/computer-aided manufacturing (CAD/CAM) system (Dassautt Systems, Suresnes, France). Figure 6 shows the entire tool surface described with 31,800 nonparametric patches. In the case of complex large-scale problems, the consuming time of contact treatment with nonparametric scheme is 4 to 5 times shorter than parametric scheme (Ref 12). Figure 7 shows the photograph of the deformed experimental shape at the final punch stroke. In actual practice, the product contains embossed reinforcements to impose rigidity in the middle part of the product and has draw beads. In the simulation, however, the tool was simplified by ignoring the draw beads. For the dynamic explicit simulations, three-node damping energy augmented BEAM element is used. The blank has an original rectangular shape of 1020 by 700 mm and 2400 triangular elements are employed.

The material and process variables used in the analysis are as follows:

- Initial sheet thickness, 0.8 mm
- Stress-strain characteristics, $\bar{\sigma} = 526.0\ (0.0074 + \bar{\varepsilon})^{0.239}$ MPa
- Young's modulus, $E = 2 \times 10^5$ MPa
- Lankford value for normal anisotropy, $r = 1.79$
- Coulomb coefficient of friction, $\mu = 0.1$
- Blankholding force, 890 kN

Coulomb forces are computed and assigned to these nodes. The explicit analysis is carried out with a constant punch velocity of 10 m/s. This punch velocity of 10 m/s, which does not affect solution reliability and is able to provide economic analysis, is chosen from the numerical tests of various punch speed. In the same way, for economic analysis the mass-scaling scheme in which 50 times the real density, which does not affect solution reliability, is employed. The velocity scaling and mass scaling methods have identical effects on solution time

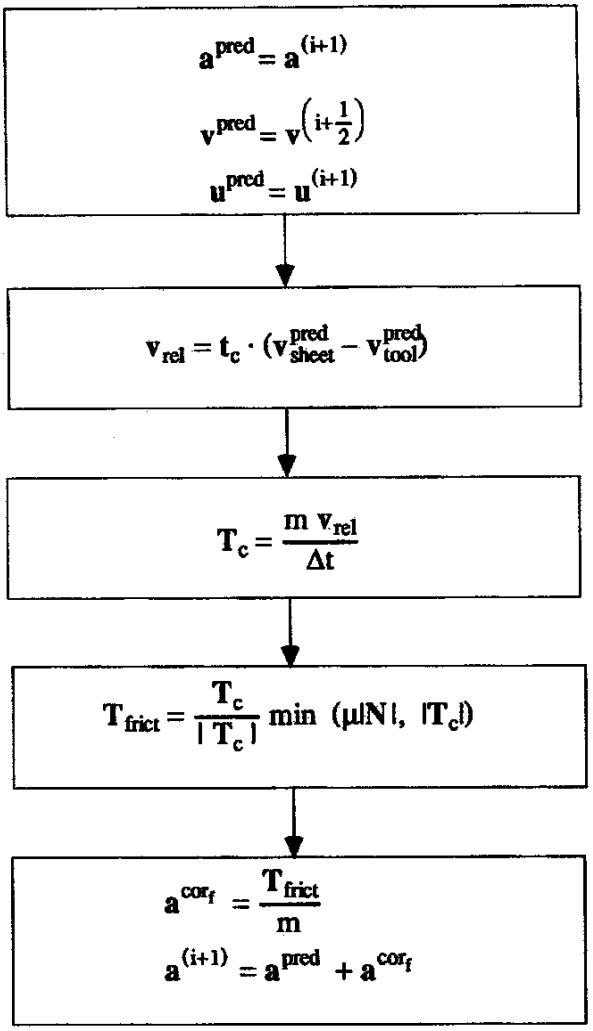


**Fig. 5** Flow chart for friction force calculation and stick/slip check

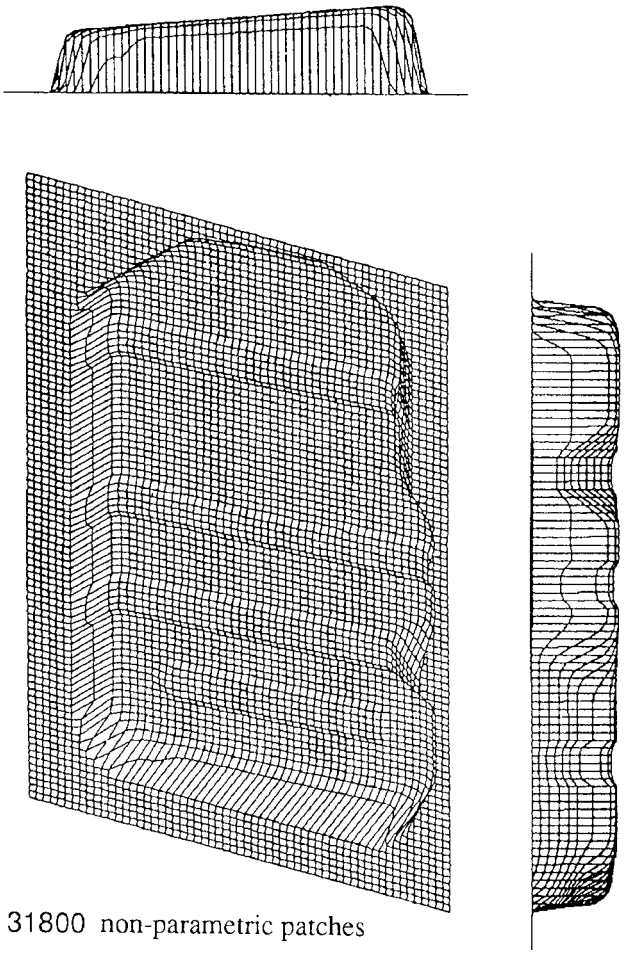


**Fig. 6** Schematic view of the nonparametric tool surfaces for fuel tank stamping

and accuracy in attempting to find a static solution using a dynamic explicit formulation from simulation results because of not using the rate-dependent material. If the rate-dependent material is used, the effects of the two scaling methods may behave differently. Figure 8 shows the comparison of the deformed edge contour predicted by the present analysis with the experimental results. The edge contour is somewhat different from the experimental result. This discrepancy is partly due to the lack of draw beads. Figure 9 shows the deformed configuration and thickness strain distribution by the dynamic explicit analysis at the punch stroke of 113 mm. This dynamic explicit analysis predicts well the most fragile region, which has a steep slope and sharp corner as shown in Fig. 7. To investigate the simulated results in more detail, the thickness strain distribution at an arbitrarily chosen section is compared with the experimental results in Fig. 10. The overall tendency of strain distribution is similar to the experimental results. However, a little higher strain level in the dynamic explicit analysis is obtained because of the faster punch velocity and the mass scaling scheme employed for the efficient analysis. The deviation can be considered from the introduction of many assumptions for the efficient and simple analysis, the limitation of analysis code itself, the measurement error of experimental results, and so forth. The whole computation time of the dynamic explicit elastic-plastic scheme takes about 4 h in HP/730 workstation (Hewlett Packard Co.). From the above example, the developed dynamic explicit elastic-plastic scheme has been successfully applied to the difficult and complicated three-dimensional automotive body panel stamping problems.

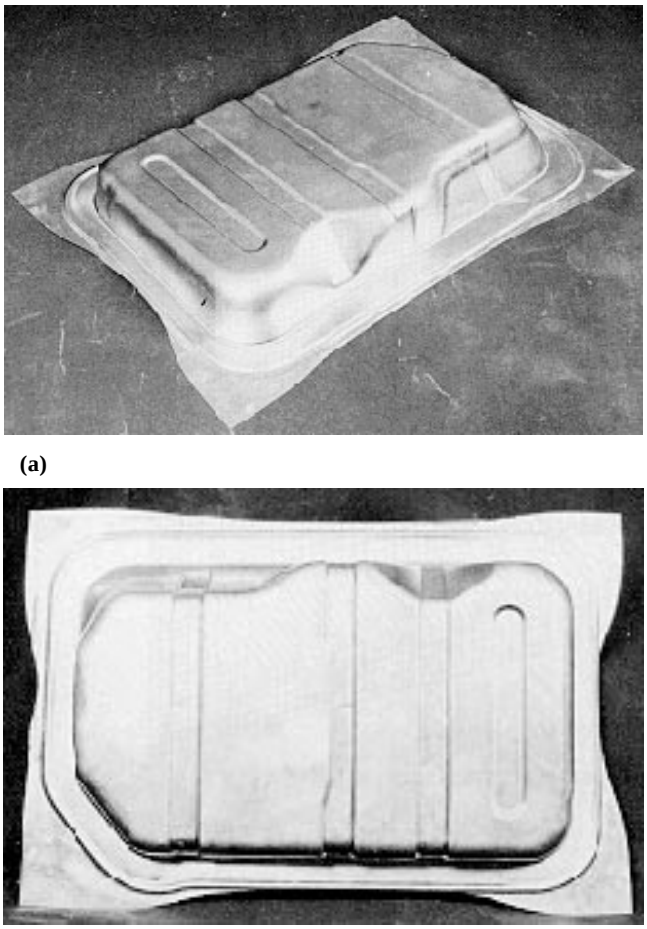

**(a)**

**(b)**

**Fig. 7** Experimental specimens of a fuel tank stamping

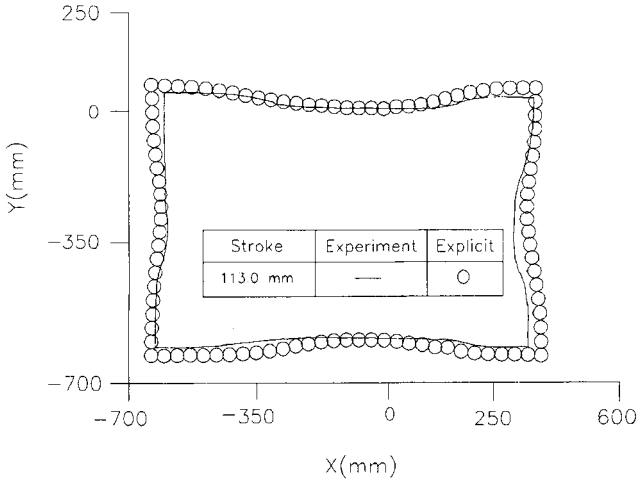


**Fig. 8** Comparison of the simulated results with the experiment for the deformed edge shape: a fuel tank stamping process

### *4.2 Deep Drawing of a Rear Hinge*

The rear hinge is one of the important sheet metal parts that make up the body of a car and is one of difficult-to-form sheet parts because it has very complex geometry, steep slope, and sharp edge and corners. The raw computer-aided engineering (CAE) surface data are constructed using the commercial CAD system CATIA. A special conversion module that can generate a rectangular array of grid points from the raw CAD surface data is used for the nonparametric patch approach. The blank has an original rectangular shape of 890 by 512 mm. Unlike the other sheet metal forming processes, the stamping process of a rear hinge consists of two stages. In the first stage, the initial sheet blank is held by the blank holder, that is, the binder surfaces, and in the second stage it is further formed into the final shape of the part. The initial sheet blank at the holding stage has

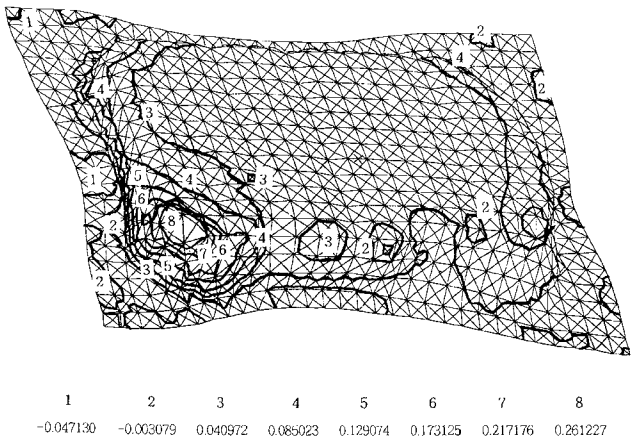


**Fig. 9** Thickness strain distribution and deformed configuration of a fuel tank predicted by the dynamic explicit elastic-plastic analysis at the final stage

often been called binder wrap. Thus, the binder wrap analysis is an indispensable step for the stamping analysis, since it provides such important data for stamping analysis as prediction of initial punch contact, draw depth, and so forth. In the work described in this article, the binder-wrap analysis, which is considered the nonlinear elastic finite element method, and the nonparametric patch approach is performed (Ref 13). The reason for using the nonlinear elastic finite element method is that the elastic-plastic finite element method requires a large amount of computational time and does not render any difference in the shape of the binder wrap. Therefore, the nonlinear elastic finite element method is more effectively applicable, and the nonparametric patch approach can save much computational time.

The material and process variables used in the analysis are:

- Initial sheet thickness, 1.2 mm
- Sheet material, cold-rolled steel
- Stress-strain characteristics, $\bar{\sigma} = 575.0\ (0.006 + \bar{\varepsilon})^{0.21}$ MPa
- Young's modulus, $E = 2 \times 10^5$ MPa
- Lankford value, $r = 1.88$
- Coulomb coefficient of friction, $\mu = 0.1$
- Blankholding force, 800 kN

Coulomb forces are computed and assigned to these nodes. For this analysis, 1904 nodes and 3680 triangular damping energy augmented BEAM elements are employed. Figure 11 shows the schematic view of the tool surfaces in the case of nonparametric patch approach in which 23,432 nonparametric patches are used to describe the punch and the die. Figure 12 shows the photograph of the deformed experimental shape at the final punch stroke. In actual practice, the product contains draw beads. In the simulation, however, the tool was simplified by ignoring the draw beads. The explicit analysis was carried out with a constant punch velocity of 10 m/s. This punch velocity of 10 m/s, which does not affect solution reliability and is able to provide economic analysis, is chosen. In the same way, for efficient analysis the mass-scaling scheme in which 50 times the real density, which does not affect solution reliability, is employed. Figure 13 shows the comparison of the deformed edge contour predicted by the present analysis with the experimental results. The edge contour is somewhat different from the experimental result. This discrepancy is partly due to the lack of draw beads. Figure 14 shows the deformed configuration and thickness strain distribution by the dynamic explicit analysis at the final configuration (punch stroke = 122 mm). The possibility of fracture in side-wall region is higher than in the upper region because it is in plain strain state even though those region are in same strain level. This dynamic explicit analysis predicted well the most fragile region. To investigate the simulated results in more detail, the thickness strain distribution at an arbitrarily chosen section was compared with the experimental results in Fig. 15. The overall tendency of strain distribution is similar to the experimental results.

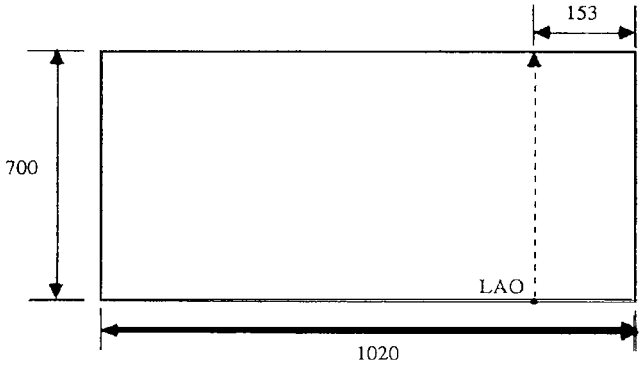


**(a)**

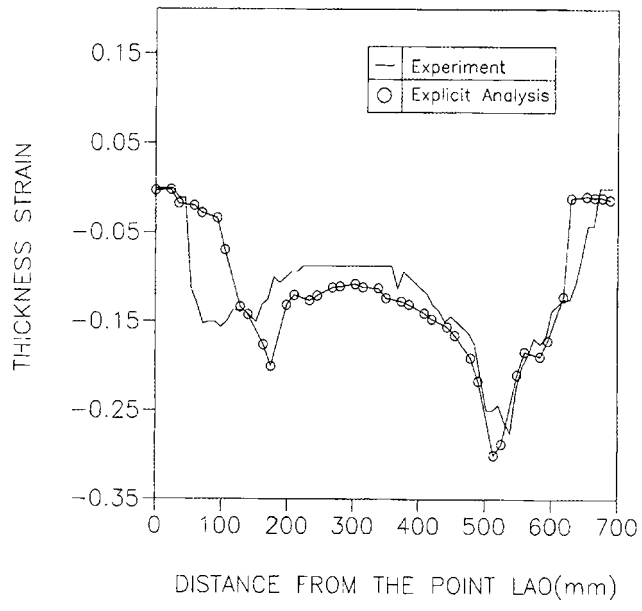


**(b)**

**Fig. 10** Thickness strain distribution for a fuel tank stamping process. (a) Baseline on initial sheet blank for strain distribution measurement. (b) Comparison of thickness strain distribution on the line

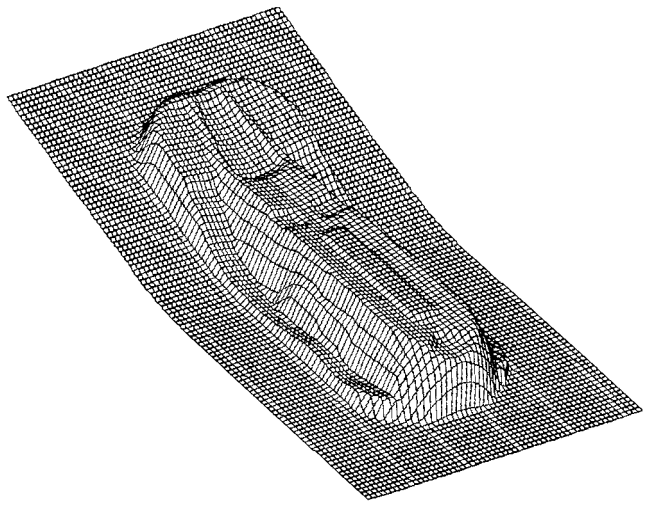


**Fig. 11** Schematic view of the nonparametric tool surfaces for rear hinge stamping

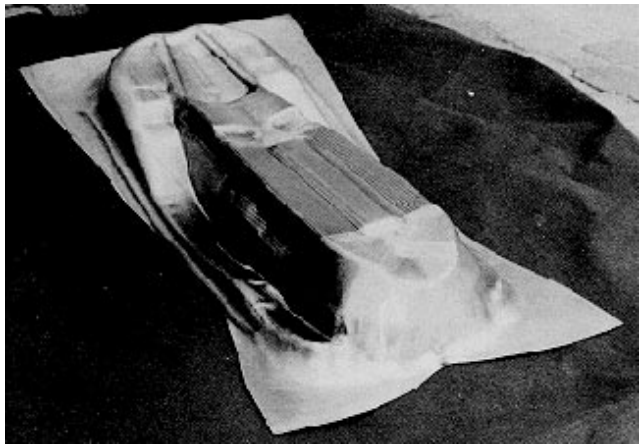

**(a)**

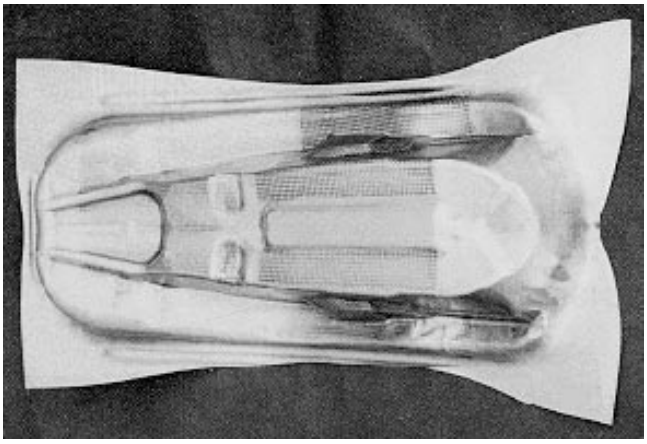

**(b)**

**Fig. 12** Experimental specimens of a rear hinge stamping

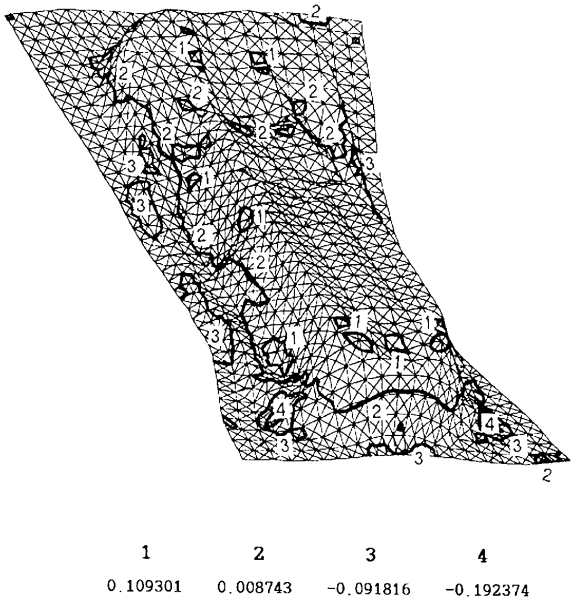


**Fig. 14** Thickness strain distribution and deformed configuration of a rear hinge predicted by the dynamic explicit elastic-plastic analysis at the final stage

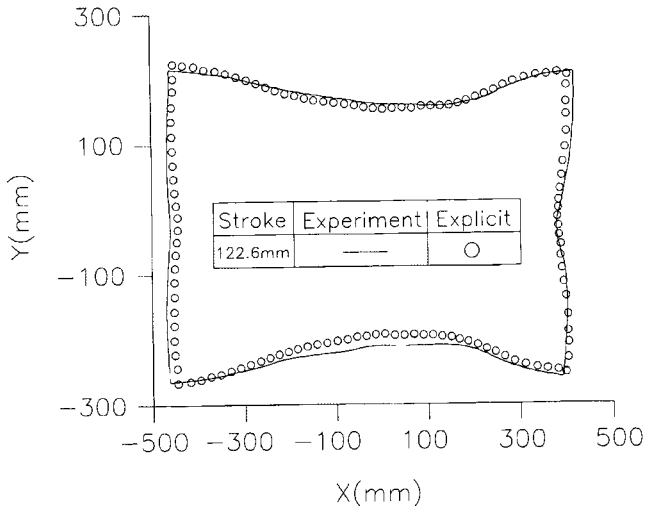


**Fig. 13** Comparison of the simulated results with the experiment for the deformed edge shape: a rear hinge stamping process

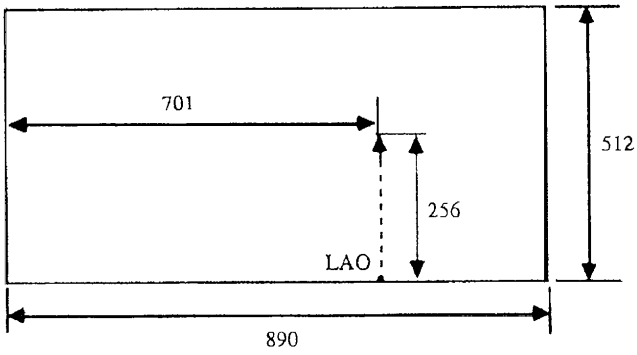


**(a)**

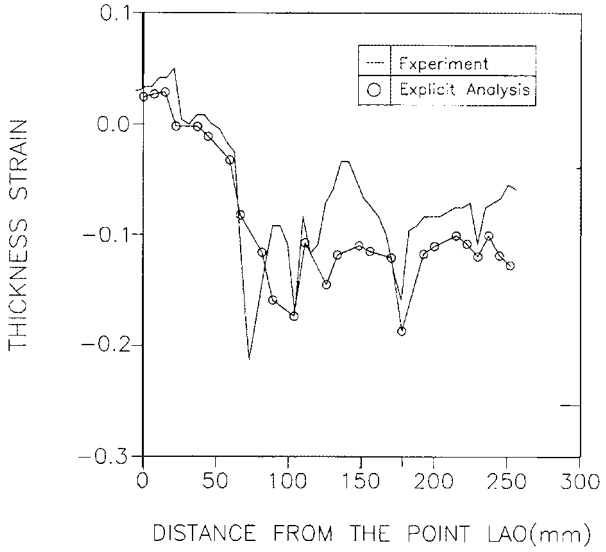


**(b)**

**Fig. 15** Thickness strain distribution for a rear hinge stamping process. (a) The baseline on initial sheet blank for strain distribution measurement. (b) Comparison of thickness strain distribution on the line

However, a little higher strain level in the dynamic explicit analysis is obtained because of the faster punch velocity and the mass-scaling scheme employed for the efficient analysis. The deviation might be considered to originate from the introduction of many assumptions for the efficient and simple analysis, the limitation of analysis code itself, the measurement error of experimental results, and so forth. The whole computation time of the dynamic explicit elastic-plastic scheme took about 8.5 h on a CRAY C90 (Silicon Graphics, Inc.). From the analysis, it is found that the dynamic explicit elastic-plastic method can be effectively applied to the huge and extremely difficult problems of automotive body panel stamping.

## 5. Conclusions

The performance of the elastic-plastic dynamic explicit algorithms is investigated, and the numerical results are compared to the experimental results with good agreement. Deep drawings with complex irregular die geometries such as forming of a fuel tank and a rear hinge are simulated. Provided that the overall numerical model is properly derived, the authors have shown that the elastic-plastic dynamic explicit formulation is an accurate, efficient, and wide-ranging tool for simulation of complex automotive body panel stamping problems.

In sheet metal forming, the amount of elastically recovered displacement is relatively large, even though the elastically recovered strain is small, because the dimension of thickness is much smaller as compared with other dimensions of the sheet metal. Highly nonlinear analysis of sheet forming is, by the nature of the process modeled, not very stable. The elastic-plastic model is considered to be more numerically stable since it includes elastic effects. During sheet forming, especially in complex deep drawing, relatively large parts of the sheet cease to be plastically deformed.

### References


1. C.H. Lee and S. Kobayashi, New Solutions to Rigid-Plastic Deformation Problems Using a Matrix Method, *J. Eng. Ind. (Trans. ASME)*, Vol 95, 1973, p 865-873
2. N.M. Wang and B. Budiansky, Analysis of Sheet Metal Stamping by a Finite Element Method, *J. Appl. Mech.*, Vol 45, March 1978, p 73-82
3. H.B. Shim and D.Y. Yang, An Elastic-Plastic Finite Element Analysis on Hydrostatic Bulging of Rectangular Diaphragms by Using Layered Degenerated Shell Elements, *Int. J. Mech. Sci.*, Vol. 32, 1990, p 49-64
4. N.M. Wang and S.C. Tang, Analysis of Bending Effects in Sheet Forming Operations, *Int. J. Numer. Methods Eng.*, Vol 25, 1988, p 253-267
5. K. Mattiason, Numerical Simulation of Stretching Processes, SIMOP-I, *Proc. of the First Int. Workshop*, K. Lange, Ed., Stuttgart, 1985, p 170-213
6. D.Y. Yang, D.W. Jung, I.S. Song, D.J. Yoo, and J.H. Lee, Comparative Investigation into Implicit, Explicit and Iterative Implicit/Explicit Schemes for the Simulation of Sheet-Metal Forming Processes, *J. Mater. Process. Technol.*, Vol 50, 1995, p 39-53
7. D.J. Yoo, I.S. Song, D.Y. Yang, and J.H. Lee, Rigid-Plastic Finite Element Analysis of Sheet Metal Forming Processes Using Continuous Contact Treatment and Membrane Elements Incorporating Bending Effect, *Int. J. Mech. Sci.*, Vol 36 (No. 6), 1994, p 513-546
8. J.C. Nagtegaal and L.M. Taylor, Comparison of Implicit and Explicit Finite Element Methods for Analysis of the FE-Sim. of 3-D Sheet Metal Forming Processes, *Automotive Ind. Conf.*, J. Reissner, et al., Ed., VDI Verlag, Dusseldorf, 1991
9. ABAQUS/Explicit: User's Examples and Theory Manuals, Hibbitt, Karlsson and Sorensen, 1991
10. E. Hinton, T. Rock, and O.C. Zienkiewicz, A Note on Mass Lumping and Related Processes in the Finite Element Method, *Earthquake Eng. Struct. Dynamics*, Vol 4 (No. 3), 1976, p 145-149
11. K.S. Surana, Lumped Mass Matrices with Non-Zero Inertia for General Shell and Axisymmetric Shell Elements, *Int. J. Numer. Methods Eng.*, Vol 12 (No. 11), 1978, p 1635-1650
12. D.J. Yoo, "Analysis of Three-Dimensional Sheet Metal Forming Processes Using Continuous Surface and Contact Treatment," Ph.D. thesis, Korea Advanced Institute of Science and Technology, 1994
13. I.S. Song, D.J. Yoo, J.W. Yoon, D.Y. Yang, H. Huh, and J.H. Lee, Finite Element Analysis and Design of Binder Wraps for Automobile Sheet Metal Parts Using Surface Boundary Condition, *J. Mater. Eng. Perform.*, Vol 4 (No. 5), 1996, p 593-598